

## Photovoltaic chimney

### Thermal modeling and concept demonstration for integration in buildings

Ortiz Lizcano, Juan Camilo; Haghghi, Zoheir; Wapperom, Sander; Infante Ferreira, Carlos; Isabella, Olindo; van den Dobbelsteen, Andy; Zeman, Miro

**DOI**

[10.1002/pip.3194](https://doi.org/10.1002/pip.3194)

**Publication date**

2019

**Document Version**

Final published version

**Published in**

Progress in Photovoltaics: research and applications

**Citation (APA)**

Ortiz Lizcano, J. C., Haghghi, Z., Wapperom, S., Infante Ferreira, C., Isabella, O., van den Dobbelsteen, A., & Zeman, M. (2019). Photovoltaic chimney: Thermal modeling and concept demonstration for integration in buildings. *Progress in Photovoltaics: research and applications*, 28 (2020)(6), 465-482.  
<https://doi.org/10.1002/pip.3194>

**Important note**

To cite this publication, please use the final published version (if applicable).  
Please check the document version above.

**Copyright**

Other than for strictly personal use, it is not permitted to download, forward or distribute the text or part of it, without the consent of the author(s) and/or copyright holder(s), unless the work is under an open content license such as Creative Commons.

**Takedown policy**

Please contact us and provide details if you believe this document breaches copyrights.  
We will remove access to the work immediately and investigate your claim.

# Photovoltaic chimney: Thermal modeling and concept demonstration for integration in buildings

Juan Camilo Ortiz Lizcano<sup>1</sup>  | Zoheir Haghighi<sup>2</sup> | Sander Wapperom<sup>1</sup> |  
Carlos Infante Ferreira<sup>3</sup> | Olindo Isabella<sup>1</sup> | Andy v. d. Dobbelsteen<sup>2</sup> | Miro Zeman<sup>1</sup>

<sup>1</sup> Photovoltaic Materials and Devices, Delft University of Technology, Delft 2628CD Zuid Holland, The Netherlands

<sup>2</sup> Architecture Faculty, Delft University of Technology, Delft 2628 BL Zuid Holland, The Netherlands

<sup>3</sup> Process and Energy, Delft University of Technology, Delft 2628 CB Zuid Holland, The Netherlands

## Correspondence

Juan Camilo Ortiz Lizcano, Photovoltaic Materials and Devices, Delft University of Technology, Delft, Zuid Holland, 2628CD, The Netherlands.

Email: J.C.OrtizLizcano@TUDelft.nl

## Present Address

Juan Camilo Ortiz Lizcano, Mekelweg 4, 2628 CD, Delft, The Netherlands.

## Abstract

This work presents the concept of a photovoltaic (PV)-powered solar chimney. We modeled and experimentally studied the integration of a PV system within a naturally ventilated façade (NVF), attempting to use the inherent cavity as a ventilation channel to transfer heat. Thermodynamic models were created to study the thermal and, therefore, the electrical performance of a PV system installed at different positions within the cavity of the NVF. An experimental setup of the PV chimney was manufactured to validate the computational models. Results show low root mean square error (RMSE) values for the prediction of the mass flow and the temperature of the different materials considered in the chimney. A basic sensitivity analysis was performed to find the best position of the PV modules within the chimney for a three-story household in the Netherlands. Optimization showed that with a cavity depth of 0.2 m with PV modules located at the front layer, the electric annual yield is maximized. For the same cavity depth, placing the modules in the middle significantly increases heat flow production, albeit with a reduction on electrical performance.

## KEYWORDS

PV façade, PV integration, solar chimney, thermal model

## 1 | INTRODUCTION

During the last years, photovoltaics (PV) has experienced significant growth in technological development, installed capacity, and cost reduction. In terms of PV technology today, almost 20 different PV

**Abbreviations:** MDF, medium-density fiber; NVF, naturally ventilated façade; POA, plane of array irradiance; PVF, photovoltaic module located at the front of the chimney; PVI, photovoltaic module located inside the cavity of the chimney.

Juan Camilo Ortiz Lizcano, Zoheir Haghighi, and Sander Wapperom contributed equally to this work.

cell technologies are available, and cell efficiency has reached 26.7% with mono-crystalline silicon cells under laboratory conditions.<sup>1</sup> This means that most of the absorbed irradiance is lost as heat. For this reason, thermal management of PV systems is becoming a topic of utmost interest. Increasing operating temperatures have a significant impact on the electric yield of a PV module<sup>2</sup> and lead to faster degradation of PV cells and reduction of service of life.

Considering the development of PV modules for urban environments and the concerns raised on the topic of urban heat islands (UHIs), heat management of integrated PV is essential. Modules

This is an open access article under the terms of the Creative Commons Attribution-NonCommercial-NoDerivs License, which permits use and distribution in any medium, provided the original work is properly cited, the use is non-commercial and no modifications or adaptations are made.

© 2019 The Authors. Progress in Photovoltaics: Research and Applications published by John Wiley & Sons, Ltd.

placed in cities and urban environment should be considered as a heat source in addition to electrical energy producing technology. This created a new trend: the development of hybrid applications with PV technology in order to extract heat from the PV modules (eg, PV thermal [PVT]).<sup>3</sup>

Over the last decades, high-rise buildings have become increasingly popular in the highly dense urban environment. Concern about climate change and the urgency to make the energy transition happen from fossil to renewable led to continuous effort to achieve the nearly zero-energy target in Europe. However, for buildings with more than three stories, it is not feasible to merely rely on the limited roof area.<sup>4,5</sup> International Energy Agency (IEA) indicates that incorporation of building-integrated photovoltaics (BIPV) on building façades only may increase PV-suitable surfaces in buildings by about 35%.<sup>6</sup>

Recently, an approach for producing natural ventilation from the vertical surfaces, known as solar chimney,<sup>7</sup> is gaining popularity. The solar chimney has been tested and placed in many projects,<sup>7</sup> and it is considered effective passive heating, cooling, and ventilation approaches for buildings.

In this work, the idea of placing a PV module inside the cavity of a solar chimney is explored. The PV module would function as of black surface inside the cavity and can help to create a buoyancy effect. The thermodynamic behavior of this system is modeled in MATLAB and validated with an experimental prototype. The model presents the performance of the system in different configurations and allows to find the most optimum geometry (cavity depth, height, and length) with respect to the energy performance of buildings, taking into consideration heating, ventilation, and electricity production.

## 2 | MODELING OF A PV CHIMNEY FAÇADE

Naturally ventilated façades (NVFs) are designed to increase the energetic performance of buildings. These devices use the incident solar irradiance to create a temperature profile from the bottom to the top of the building. This profile generates an airflow within the cavity, which is driven by buoyancy forces created owing to temperature difference between the contained air and the ambient air. This flow can be used, among others, for ventilation purposes, thus reducing the demand of electricity. Details for different NVF concepts can be found in Oesterle et al.<sup>8</sup>

Different approaches to model the behavior of a NVF have been proposed during the last decade. Analytical models like the one by Von Grabe,<sup>9</sup> nondimensional analysis,<sup>10</sup> one-dimensional lumped element as described in Rheault and Bilgen,<sup>11</sup> nodal network models as used in Gratia and De Herde<sup>12</sup> and Ioannidis et al,<sup>13</sup> and computational fluid dynamics (CFD) methods such as those by De Gracia et al.<sup>14</sup>

This work uses a model based on a combination of a control volume model (CVM) and an analytic mass flow model created entirely in MATLAB and will be briefly explained in Section 2.2. User inputs of the CVM are meteorological data of the location, the chimney layout (height, width, depth, and building materials), the total surface of

the PV façade, the PV module specifications, and the orientation in which the chimney is meant to be installed. Given the overall layouts of NVF, all heat transfer mechanisms are described in 2D. It has been proven that such an approach yields accurate results for aspect ratios (height divided by depth) larger than 2. Wong et al<sup>15</sup> demonstrated an error of 4% of 2D models that fulfill this condition when compared with more sophisticated 3D models of the same geometry. In general terms, the model works as follow: To find the heat flux transferred to the airflow, the finite volume method is used. The increase in surface temperature due to the irradiance reaching the chimney is found. The combined convective heat transfer from the surfaces to the airflow is calculated and used as input in the mass flow model. Both models are solved by iteration.

### 2.1 | Irradiance model

The model uses the meteorological data as one of its main inputs. The user can provide a typical meteorological year (TMY) file to provide hourly data of global horizontal irradiance (GHI), diffuse horizontal irradiance (DHI), and direct normal irradiance (DNI). The MATLAB model has embedded a solar position calculator following the method described in Smets et al.<sup>16</sup>

The contribution on the plain of array irradiance over a vertical layer from the direct component of the irradiance is denoted by Equation (1).

$$G_L^{\text{dir}} = \text{DNI} \times \cos(\theta), \quad (1)$$

where the cosine parameter represents the angle of incidence on the plain of array, denoted by Equation (2).

$$\cos(\theta) = \cos(A_{TS}) \times \cos(A_{ZL} - A_{ZS}). \quad (2)$$

Diffuse irradiance component contributions are calculated via Equation (3):

$$G_L^{\text{dif}} = \frac{1}{2} \times \text{DHI}, \quad (3)$$

which represents the contribution of the diffuse component for a free horizon on a vertical surface. The contribution of the ground irradiance was considered by

$$G_L^{\text{gr}} = \frac{1}{2}(\Lambda)(\text{GHI}), \quad (4)$$

where  $\Lambda$  represents the value of the albedo of the ground. The sum of the values obtained in Equations (1), (3), and (4) gives the plane of array irradiance on a layer in the chimney before reflectance losses:

$$G_L^{\text{POA}} = G_L^{\text{dir}} + G_L^{\text{dif}} + G_L^{\text{gr}}. \quad (5)$$

### 2.2 | Control volume method

The model divides the geometry of the PV chimney into finite volumes. These are defined by the number of vertical volumes and the

number of horizontal volumes per layer, both of which can be defined by the designer of the chimney. The number of horizontal volumes on each layer must be equal for all of the layers. Air layers have only one horizontal control volume, given the nature of the mass flow model as described in Section 2.2.3. An adjustable material database is included in the model. This database can be extended, and the user can choose any material present in the database to design the chimney.

An energy balance is created for each control volume and surface created in the model. Temperature calculations are done by the solving the energy equations at each layer using a first-order implicit central difference scheme. Since mass flow is considered as one-dimensional upward flow, a first-order upwind scheme is used for the calculation of heat transfer by the movement of air. Once all the equations are obtained, a matrix  $A$  and a vector  $b$  are created as described by Equation (5). In this way, Gaussian elimination can be used to solve the set of equations and obtain the temperature at each control volume, thus defining a temperature profile over the entire chimney.

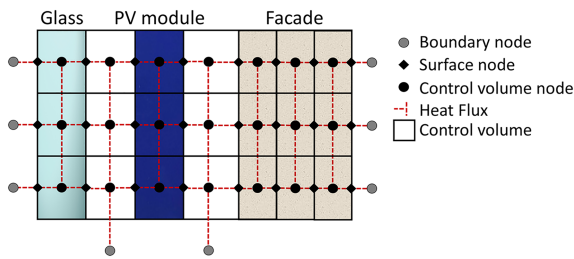
$$A \times T = b. \tag{6}$$

Figure 1 shows a schematic representation of how the model constructs the matrices to perform the iterative calculations used to find the heat fluxes and surface temperatures. The PV panel is considered to be installed inside the cavity of the chimney, and its position will be moved to find the best energy performance for a given location and energy need.

### 2.2.1 | Optical losses and PV power calculation

The first calculations performed by the model are the optical losses on the incident irradiance into the first glass layer of the chimney. Solar radiation and grey body radiation are treated separately.

The first reflection on the front glass is calculated considering the angle of incidence of light in the plane of array (determined by Equation 1) and the refractive index of glass, here considered constant over all the wavelengths and equal to 1.52.<sup>17</sup> Backside reflectances are not considered in this model, as explained by Figure 2. Reflective losses are found first by averaging the reflectance of the perpendicular



**FIGURE 1** The user can define the amount of different vertical volumes and the horizontal control volumes per layer. The graph describes only three different vertical volumes and one horizontal volume per layer. Interaction between surface, center, and boundary nodes is also shown as the modeled heat fluxes [Colour figure can be viewed at wileyonlinelibrary.com]

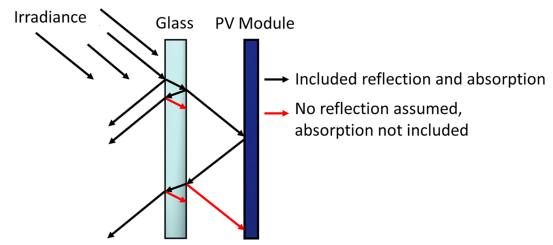


**FIGURE 2** Reflectance of light on the air/glass/air/PV system. The red arrows highlight those omitted on the model, and the black ones those that are calculated. PV, photovoltaics [Colour figure can be viewed at wileyonlinelibrary.com]

( $r_p$ ) and the parallel ( $r_s$ ) polarized light, described by the following equations.

$$r_s = \frac{r_{i1} \cos \theta_t - r_{i2} \cos \theta_t}{r_{i1} \cos \theta_t + r_{i2} \cos \theta_t}, \tag{7}$$

$$r_{po} = \frac{r_{i1} \cos \theta_t - r_{i2} \cos \theta_i}{r_{i1} \cos \theta_t + r_{i2} \cos \theta_i}, \tag{8}$$

where  $r_{i1}$  and  $r_{i2}$  are the refractive indexes of the incident medium (air) and the glass, respectively, and  $\theta_t$  is the angle of transmittance, which can be calculated via the Snell law by

$$\theta_t = \arcsin\left(\frac{r_{i1}}{r_{i2}} \sin \theta_i\right).$$

Lastly, the total reflectance is found using Equation (9):

$$R = 0.5(r_s^2 + r_{po}^2) \tag{9}$$

Since the refractive index of air is considered equal outside and inside the chimney, the angle of incidence of light on the PV modules will be equal to the angle of incidence of light in the front glass. The effective irradiance reaching each layer is then defined by

$$I_L = G_L^{POA} - R_L^{losses}. \tag{10}$$

The absorbed irradiance is considered as a source of heat ( $\dot{q}_{abs}$ ) on each control volume ( $N$ ) of the different layers. On general terms, this quantity is calculated by

$$\dot{q}_{absN} = I_N(1 - \exp(-\alpha d)), \tag{11}$$

where  $\alpha$  is the extinction coefficient of the material (which for glass was considered constant and equal to  $8.7 \text{ m}^{-1}$ ) and  $d$  is the thickness of the layer and in the model also equal to the control volume depth.

Transmitted irradiance that reaches the next control volume is calculated by

$$I_{N2} = I_{N1} - \dot{q}_{absN1}, \tag{12}$$

where subscripts 1 and 2 denote two consecutive control volumes within any layer of the chimney. For the case of a layer, like the solar cells within the PV module located inside the cavity, this is expressed

as

$$I_{sc} = I_{gl} - \dot{q}_{absgl}. \quad (13)$$

Notice that this effective irradiance  $I_{sc}$  also considers the reflectance losses on the front surface of the module, as shown in Figure 2. Once its value is found, the model calculates the PV power. In this study, the PV module has the following characteristics: (a) front and back layers are glass of 4-mm thickness; (b) the encapsulant (ethyl vinyl acetate [EVA]) is assumed as 1 mm thick and with the same optical and thermal characteristics of the glass, 15.24-cm mono-cSi solar cells with a standard test condition efficiency of 17%.

The power delivered by the PV module is adjusted for different angles of incidence of light and different operating cell temperature following the works of Haedrich et al.<sup>18</sup> and Cotfas et al.,<sup>19</sup> respectively, by altering the efficiency  $\eta$ . Then the power is calculated by

$$P_{PV} = I_{sc} \times \eta. \quad (14)$$

In the model, the PV module is divided into a number of control volumes equal to those chosen by the user. The middle volume is used to model the solar cells, and it is considered as a perfect absorber, meaning that no irradiance reaches the building layer. The effective irradiance on the solar cell is given by Equation (13). The heat flux on the solar cells ( $\dot{q}_{sc}$ ) is then defined as

$$\dot{q}_{sc} = I_{sc} - P_{PV}. \quad (15)$$

## 2.2.2 | Heat transfer coefficient

### Convection

Convective heat transfer occurs on all the different layers of the chimney; at the boundary between ambient air and the front glass, at the back boundary of the front glass and the air within the cavity, and on both boundaries of the PV with the air within the cavity. The most suitable equations for the Nusselt number to model the air within the chimney were identified to be

$$Nu_x = 0.406Gr_x^{1/4} \quad Gr_x < 10^9, \quad (16)$$

for laminar flow and

$$Nu_x = 0.1(Gr_x Pr)^{1/3} \quad Gr_x \geq 10^9, \quad (17)$$

for turbulent flow, where  $x$  is the vertical distance along the walls. The Grashof number is calculated depending on the average temperature of the contained air and the boundary of the studied layer. The convective heat transfer coefficient is then calculated by

$$h_c = \frac{Nu_x k}{x}, \quad (18)$$

where  $\kappa$  is the thermal conductivity of air. Once  $h_c$  is known, the heat flux from the boundary layer to the air is known, and the mass flow can be calculated. However, the mass flow also affects the

convective heat transfer coefficient. Iteration is required to find the right value of  $h_c$ .

### Radiation

Since any object with a temperature above 0 K irradiates heat, the model makes a distinction between solar radiation and grey body radiation. For the latter, the radiation transmitted to the environment is defined by

$$Q_{12} = F_{12} A_1 \epsilon_1 \sigma (4\bar{T}^3) (T_1 - T_2), \quad (19)$$

where  $F_{12}$  is the view factor of layer 2 seen from layer 1.  $A_1$  is the area of layer 1,  $\epsilon_1$  is the emissivity of the material, and  $\sigma$  is the Stefan-Boltzman constant.  $\bar{T}$  is the average temperature of layer 1 and layer 2, and  $T_1$  and  $T_2$  are the temperatures of layers 1 and 2, respectively. The radiative heat transfer coefficient is, therefore, defined by

$$h_r = F_{12} \sigma \epsilon (4\bar{T}^3). \quad (20)$$

To calculate the view factors, the following equation is used:

$$F_{12} = \left( 1 + \left( \frac{d}{H} \right)^2 \right)^{0.5} - \frac{d}{H}, \quad (21)$$

where  $d$  is the depth of the channel and  $H$  is the total height. In the model, the view factor is equally divided over the number of vertical control volumes, as follows:

$$F_{1N} = \frac{F_{12}}{N_v}. \quad (22)$$

The façade to environment view factor can be calculated by subtracting each layer view factor from the unity.

### Conduction

For conduction, the 2D Fourier law is used, which is defined by

$$\rho c_p \frac{\partial T}{\partial t} = \frac{\partial}{\partial x} \left( k \frac{\partial T}{\partial x} \right) + \frac{\partial}{\partial y} \left( k \frac{\partial T}{\partial y} \right) + Q_{src}, \quad (23)$$

where  $Q_{src}$  is heat generated by a source.  $c_p$  is the specific heat,  $\rho$  is the density, and  $k$  is the thermal conductivity. In this model, the thermal properties of solids are considered constant.

## 2.2.3 | Mass flow model

There are three different analytical methods for calculation of the mass flow. The first one averages the temperature of the complete air channel, which is often referred to as the single zone model (see Figure 3A). In this model, the pressure that drives the flow is calculated based on the difference between the channel temperature and the contained air temperature. The second model takes the variation of temperature with height into account and is referred to as the stratified model (see Figure 3B). The driving pressure difference is

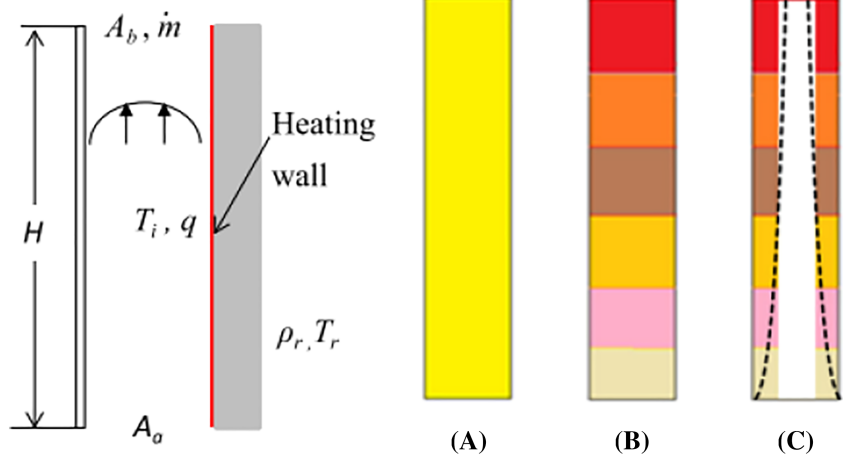


**FIGURE 3** Different analytic models can be used to calculate the mass flow due to buoyancy in a channel: A, a single zone model; B, the stratified model<sup>20</sup>; and C, the plume model.<sup>26</sup> Original source of the figure is He et al<sup>26</sup> [Colour figure can be viewed at wileyonlinelibrary.com]

calculated by integrating the density over the height of the chimney.<sup>20</sup> The resulting difference in density is used to calculate the pressure difference driving the flow.

Lastly, the plume model (shown in Figure 3C) considers both horizontal and vertical variations in temperature. The correction factors of this model were adjusted to increase accuracy and adopted in the current model. Based on the works,<sup>20-25</sup> this model yields better accuracy than its alternatives for similar cases.

The model assumes a constant plume depth. However, the value of temperature within the plume varies, except for the air contained between the plumes, which is considered constant and equal to the ambient temperature. The model aims to solve the mechanical energy balance, as represented by Equation (24) in its simplified form.

$$(\rho_e - \rho_{ch})gH = \frac{\dot{m}^2}{2A} \left( \frac{K_{in}}{\rho_e} + \frac{K_{exit}}{\rho_p} + \frac{fH}{d_h \rho_{ch}} \right). \quad (24)$$

The right side of the equation depicts the pressure loss due to inlet, outlet, and channel friction. The entrance and exit friction coefficients ( $K_{in}$  and  $K_{exit}$ ) are equal to 0.5 and 0.88, respectively. The model considers all cavity areas as equal (inlet, outlet, and shaft). The Darcy friction factor ( $f$ ) is calculated as a function of the Reynolds number, the hydraulic diameter of the plume ( $d_h$ ), and the channel area (A). The left side shows the pressure difference as a result from the variation in density.

Density at channel's exit ( $\rho_e$ ), the plume density ( $\rho_p$ ), and the mean channel density ( $\rho_{ch}$ ) are calculated using Equations (25) to (27). The Boussinesq approximation is used to calculate the density of the air in the channel and the resulting difference with the ambient air. The ideal gas law is considered for the calculation of the plume density ( $\rho = p/(RT)$ ). Finally, the channel depth ratio ( $\zeta$ ) and the weighted mean of the environmental and plume densities allow to calculate the channel density.

$$\rho_{exit} = \rho_e (1 - \beta(T_{exit} - T_e)), \quad (25)$$

$$\rho_p = \rho_e \frac{T_e}{T_{exit} - T_e} \log \frac{T_{exit}}{T_e}, \quad (26)$$

$$\rho_{ch} = \zeta \rho_p + \rho_e (1 - \zeta). \quad (27)$$

The thermal boundary layer ( $\delta_T$ ) is calculated using Equation (28), where  $Ra_H$  is obtained by the heat flux ( $\dot{q}$ ). The thermal boundary layer is then used to calculate the plume depth to channel depth ratio as shown in Equation (29). In it,  $b$  is a correction factor that is found empirically, and  $n$  is the expected boundary layer within the plume. In this work,  $n$  is always equal to 2, as the model considers each cavity of the chimney as a separate system with the middle layer (eg, the PV module) being common for each case. The plume depth to channel depth ratio is used to calculate the channel density and the hydraulic diameter of the plume. Notice that when this ratio is equal to 1, the plume model is equal to the stratified model.

$$\delta_T = 4.5H \frac{\left(1 + \frac{Pr}{7.22}\right)^{0.9}}{(Ra_H Pr)^{0.2}}, \quad (28)$$

$$\zeta = nb \frac{\delta_T}{d}. \quad (29)$$

Equations (30) to (32) show the correction factors. It can be seen that for the case of laminar flow, no correction factor is needed. Change from laminar flow to turbulent flow occurs when the value of the Reynolds number equals or exceeds 2300. In his work, He et al<sup>26</sup> proposed a number of correction factors; however, on this work, other values were deemed more suitable. These factors were optimized by reducing the root mean square error (RMSE) between experimental data and the model. An iterative process was used in which the correction factor started at a low value and was slightly increased until the RMSE reached a minimum.

$$b = 1, \text{ Re}_{ch} < 2300, \quad (30)$$

$$b = 0.00042 \text{Re}_{ch}, \text{ Ra}_H < 10^{14}, \quad (31)$$

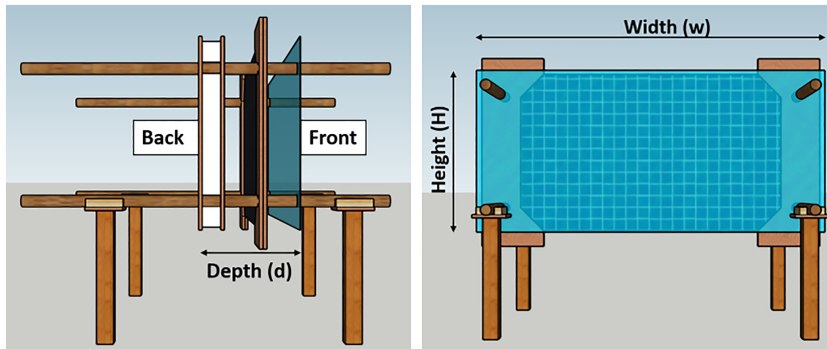


**FIGURE 4** Sketch of the setup built for the validation of the mass flow and control volume models [Colour figure can be viewed at [wileyonlinelibrary.com](http://wileyonlinelibrary.com)]

$$b = 0.000128\text{Re}_{\text{ch}}, \text{Ra}_H \geq 10^{14}. \quad (32)$$

### 3 | EXPERIMENTAL SETUP AND MEASUREMENT RESULTS

Figure 4 shows a sketch of the experimental setup without side material and sensors and without the large-area steady-state (LASS) solar simulator. The layers, from front to back, consist of glass, PV, and medium-density fiber (MDF) with insulation material. This topology will be referred to as “PV inside (PVI)” throughout the text. Another topology, without front glass, was also measured. This second layout will hence be referred to as “PV at front” or PVF. The frame is made from four cylindrical wooden poles, allowing depth adjustment of the PV module. MDF extensions were added to the front layer. This was done to prevent irradiance by passing the first layer and directly reaching subsequent layers. The built setup is depicted in Figure 5. The main measurements of the setup are listed below:

1. The maximum width was determined by the size of the PV module, which is 2 m.
2. The inlet of the chimney had the same size of the cavity, which varied according to the layout studied.
3. The inlet was located at 62.1 cm from the ground floor of the laboratory.
4. The outlet of the chimney was located at 164.1 cm from the ground.
5. The outlet had the same size as the cavity and, therefore, the inlet.
6. The distance from the outlet to the ceiling of the laboratory was 52.8 cm.

The width of the frame is an additional 0.1 m on both sides of the PV module, resulting in a total width of the structure of 2.2 m. Since other large-scale experiments with similar heights found no influence of the edges for widths of 1 m, a value of 2.2 m is considered safe from such influence.<sup>20-25,27,28</sup>

The height affects both the mass flow and the temperature distribution of the concept. Ideally, the height is as high as the façade of a building. Therefore, a large height is recommended to reduce potential scaling errors. However, in the experiment, the height was limited to the dimensions of the LASS, which stands in front of the test setup. The dimensions of the PV module available were 1.02 m by 2 m, which was placed on landscape position to ensure illumination from the LASS as homogeneously as possible. Such positioning limited the height of the remaining layers to 1.02 m, resulting in an aspect ratio of 0.5.

The channel depth was varied between 0.1 and 0.4 m in total; the aim of the experiment was to validate the model and then use it to predict the best location for a PV module.

Layer thicknesses were selected to be as close as possible to a real application. A glass-glass PV module of 8-mm thickness is used as a front or middle layer. When the PV is placed in the middle, a hardened glass sheet of 8-mm thickness is used as a front layer. Finally the back layer consisted of MDF plates of 18 mm of thickness, insulated with 60-mm-thick polystyrene to simulate an insulating building material.

The sides were closed with plastic sheets to prevent horizontal draught. Layers were placed as vertical as possible, and inclination readers were taken at each new set of data collection.

#### 3.1 | Large-area steady-state solar simulator

A LASS, developed by Eternal Sun, was used to produce irradiance. The LASS is designed to reproduce irradiance conditions similar to



**FIGURE 5** The setup was built according to the physical properties of the PV module used. Left, the setup without the front glass. The thermocouples were installed in the geometrical middle of the setup, as is also shown in Figure 6. Right, the full setup with front glass and the plastic side coverage sheets. PV, photovoltaics [Colour figure can be viewed at [wileyonlinelibrary.com](http://wileyonlinelibrary.com)]

**TABLE 1** Sensors used in the experiment depicted with the range and accuracy provided by the manufacturer

Sensor Type	Range	Accuracy
Hot sphere anemometer	0 to 10 m/s	$\pm(0.03 \text{ m/s} + 5\% \text{ of mv})$
Hot sphere anemometer	$-20^{\circ}\text{C}$ to $70^{\circ}\text{C}$	Not specified
Thermocouple T-type	$-40^{\circ}\text{C}$ to $350^{\circ}\text{C}$	Largest of $\pm 0.5$ or $\pm 0.004T$ ( $^{\circ}\text{C}$ )
GC-10 Eltek humidity sensor	0% to 100%	$\pm 2\%$
GC-10 Eltek temperature sensor	$-30$ to $65$	$\pm 0.4^{\circ}\text{C}$
Kipp & Zonen SPM10-A pyranometer	285 to 2800 nm	$<10 \text{ W/m}^2$

those of the standard for PV module testing ( $1000 \text{ W/m}^2$  in the range of 300–1200 nm). The equipment is classified as A for spectral match on the wavelength ranges of 400 to 600, and 800 to 1000 nm, and B for the remaining equipment according to the IEC 60904-9 standard. However, at wavelengths larger than 1200 nm, a significant amount of irradiance is produced by the light sources, resulting in a total irradiance of roughly  $1665 \text{ W/m}^2$  in the complete range of the sensor. The front surface of the first layer was always positioned at a distance of 0.71 m from the lamps of the LASS to produce illumination as homogeneously as possible.

### 3.2 | Measurement sensors

Four variables were monitored by the use of five different sensors. Their main characteristics are summarized in Table 1. T-type Perfluoroalkoxy (PFA)-exposed welded tip thermocouples from RS components were used to measure front and back wall temperatures at each layer. A total of seven were used on each side to measure a temperature profile. Measurements were stored by using a PicoLog TC-08 USB data logger. Ambient temperature was also measured with a fully shaded thermocouple, thus preventing any potential measurement bias.

A hot sphere anemometer was used to measure both the temperature and velocity profile of air. The latter was then used to calculate the mass flow. Both the temperature profile and the mass flow were used to estimate the convective heat flow. The sensor used was a Testo hot bulb probe with 3 mm of diameter (reference 0635 1049) alongside the Testo 445 multifunction instrument, which was used to log all the measurements.

A humidity sensor was used to measure the humidity, since relative humidity could influence the Nusselt number by up to 2% and the Prandtl number by up to 5% under the current test conditions.<sup>29</sup> Finally, a pyranometer was used to measure the irradiance incident on both the front glass and PV module of the experimental façade.

In total, 42 thermocouples, three heat flux sensors, one humidity sensor, one hot sphere anemometer, and one pyranometer were used for this experiment. All measurements were recorded using their corresponding manufacturer data logger.

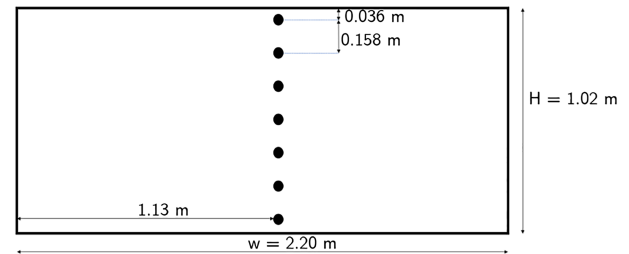


**FIGURE 6** Thermocouple (depicted by the black dots) distribution on each of the layers of the chimney; they were installed equidistant from one another and located at the center of the layers [Colour figure can be viewed at [wileyonlinelibrary.com](http://wileyonlinelibrary.com)]

### 3.3 | Sensor placement

As mentioned before, seven thermocouples were used on each of the chimney layers to produce temperature profiles. Their distribution on each of the chimney layers is shown in Figure 6. On the last layer of the PV chimney structure (the building wall), two heat flux sensors were used, replacing two thermocouples, the top and bottom ones. Humidity sensor was attached to the structure and hidden from direct irradiance from the LASS. The anemometer was located at 0.10 m below the exit of the air channel.

Before starting the complete set of measurements, three small experiments were conducted to increase the accuracy and confirm initial assumptions in the model. First, since irradiance is the driving force behind the stack effect on the chimney, its impact on the measurement of air velocity was studied. It was found that by using a time scale of 20 seconds in the value averaging, the RMSE value was below that of the equipment error. Second, the natural draught of the room was measured. It was found that values equal or below 0.2 m/s could be caused by the room and not by the stack effect on the chimney. Lastly, measurements were carried out to compare the inlet air temperature of the chimney and the ambient temperature of the room. It was confirmed that these values can be considered equal, as assumed by the thermal model.

### 3.4 | Topology measurements

Two main chimney topologies were considered for the measurements. The first one considers the PV module as the front layer of the cavity,

**TABLE 2** Topologies measured during the experiment

Topology	Distance Between First and Second Layers, m	Distance Between Second and Third Layers, m	Amount of Measurements
PVF, 0.1 m	0.1	-	3
PVF, 0.2 m	0.2	-	3
PVF, 0.4 m	0.4	-	4
PVI, 0.1, 0.1 m	0.1	0.1	2
PVI, 0.2, 0.2 m	0.2	0.2	2
PVI, 0.3, 0.1 m	0.3	0.1	2
PVI, 0.1, 0.3 m	0.1	0.3	2

Note. The second and third columns show the depth of the different cavities when the photovoltaics (PV) is either at the front (PVF) or inside (PVI).

**TABLE 3** The measured irradiance including the RMSE ( $W/m^2$ ) in front of the first layer

		Distance From the Left Side, Viewed From the Front					
		0.42 m	0.74 m	1.05 m	1.21 m	1.52 m	1.84 m
Dist. from top	0.11 m	1578±7	1651±15	1672±17	1671±5	1669±8	1533±11
	0.43 m	1603±8	1702±5	1710±1	1725±5	1705±7	1569±10
	0.59 m	1578±8	1680±5	1692±7	1702±10	1695±4	1567±17
	0.90 m	1442±16	1578±30	1568±12	1536±30	1574±19	1491±23

Note. The distance from the top and the side for each measurement is shown in the second column and the second row, respectively.

Abbreviation: RMSE, root mean square error.

henceforth known as PVF. The second considers the PV located inside the cavity, henceforth known as PVI. The distance studied, which determines the main cavity of the façade (for the PVF case) and the two sub-cavities of the chimney (for the case of PVI), is summarized in Table 2.

### 3.4.1 | Uncertainty

Bias errors were reduced by the use of automated data loggers for all the measurements, except the air velocity. This value was taken once the new position of the probe reached steady state. It was considered that the measurement could be performed once the value did not change for more than 20 seconds. Obtained data did not show any sign of bias.

Random errors were quantified via the mean squared error value (RMSE) or the standard deviation, which are equal when the bias error

is zero. Calculation of the RMSE error was done via

$$RMSE = \sqrt{\frac{1}{N} \sum_{i=1}^N (e_i - \bar{e})^2}. \quad (33)$$

### 3.4.2 | Results and analysis

#### Irradiance measurements

Irradiance measurements were carried out on 24 different points on both the front PV module, for the case of the PVF, and on the front layer of both the glass and the PV module located inside the cavity, for the PVI. Measured values are summarized in Table 3. Irradiance values are not homogeneous across the front layer of the structure. The largest vertical deviation has a value of  $147 W/m^2$ , and the largest horizontal deviation is  $157 W/m^2$ .

**TABLE 4** The measured irradiance including the RMSE ( $W/m^2$ ), 65 mm behind the glass layer

		Distance From the Left Side, Viewed From the Front					
		0.42 m	0.74 m	1.05 m	1.21 m	1.52 m	1.84 m
Dis. from top	0.11 m	1078±46	1110±6	1111±38	1115±11	1119±11	1038±27
	0.43 m	1179±52	1238±7	1224±37	1259±8	1244±4	1113±7
	0.59 m	1192±55	1256±7	1231±48	1279±9	1260±8	1128±12
	0.90 m	1169±49	1213±15	1183±42	1236±13	1235±12	1099±12

Note. The distance from the top and the side for each measurement is shown in the second column and the second row, respectively.

Abbreviation: RMSE, root mean square error.

**TABLE 5** Environment temperature and RMSE ( $^{\circ}\text{C}$ ) for all topologies

Topology	Temperature, $^{\circ}\text{C}$
PVF, 0.4 m	29.8 $\pm$ 0.2
PVF, 0.2 m	29.6 $\pm$ 0.3
PVF, 0.1 m	32.8 $\pm$ 0.4
PVI, 0.1, 0.1 m	28.9 $\pm$ 0.2
PVI, 0.2, 0.2 m	27.9 $\pm$ 0.4
PVI, 0.3, 0.1 m	29.4 $\pm$ 0.4
PVI, 0.1, 0.3 m	26.9 $\pm$ 0.4

Note. PVF means photovoltaics (PV) as front layer, and PVI means the PV located inside. The distances indicate the depth of the main cavity for the PVF case, and the first and second cavity, respectively, for the PVI case.

Abbreviation: RMSE, root mean square error.

When the mean irradiance was calculated, the values from the side edges of the layer (column 0.42 and 1.84 m in Table 3) were omitted. The reason for this is that it is considered that those values have negligible influence on the mass flow produced at the center. The obtained mean irradiance was 1665  $\text{W}/\text{m}^2$ . This high value is mainly produced by infrared emission coming from the light sources used on the LASS solar simulator, which increases the overall temperature of the layers. This produces higher Rayleigh numbers, resulting in similar flow structures found on NVF with lower irradiance but greater height.

For the case of the PVI layout, the measured irradiance on the PV module located inside the cavity allowed to quantify reflection and absorption losses on the front glass. Given that the layers had the same height and width, measurements were taken on the same locations. Table 4 shows the measured values. The average absorption on the glass was found to be 27%. This high value is explained by the amount of infrared radiation emitted by the LASS. For both the PVI and PVF layouts, the PV module was installed but not connected, modeling a  $V_{\text{OC}}$  condition.

### Environment air temperature

Table 5 summarizes the average environmental temperature measured during the different layout setups. It can be seen that there is a

**TABLE 6** Relative humidity and RMSE (%) of the environment air for all topologies

Topology	Relative Humidity, %
PVF, 0.4 m	40.1 $\pm$ 0.7
PVF, 0.2 m	32.3 $\pm$ 0.8
PVF, 0.1 m	32.5 $\pm$ 0.8
PVI, 0.1, 0.1 m	35.0 $\pm$ 0.4
PVI, 0.2, 0.2 m	25.2 $\pm$ 0.4
PVI, 0.3, 0.1 m	31.7 $\pm$ 0.5
PVI, 0.1, 0.3 m	36.2 $\pm$ 0.5

Note. PVF and PVI follow the explanation found in Table 5.

Abbreviations: PVF, photovoltaics as front layer; PVI, photovoltaics located inside; RMSE, root mean square error.

**TABLE 7** The average temperature ( $^{\circ}\text{C}$ ) readings of the thermocouples placed on the surface of each layer

Distance From Top, m	PV		MDF	
	Front T, $^{\circ}\text{C}$	Back T, $^{\circ}\text{C}$	Front T, $^{\circ}\text{C}$	Back T, $^{\circ}\text{C}$
0.04	113.1 $\pm$ 0.5	106.1 $\pm$ 0.6	61.6 $\pm$ 0.8	-
0.19	112.2 $\pm$ 0.7	108.2 $\pm$ 0.8	68.0 $\pm$ 0.8	31.0 $\pm$ 0.5
0.35	113.2 $\pm$ 0.8	107.0 $\pm$ 0.8	68.1 $\pm$ 0.8	31.1 $\pm$ 0.5
0.51	116.4 $\pm$ 0.6	106.8 $\pm$ 0.6	69.9 $\pm$ 0.8	30.6 $\pm$ 0.5
0.67	107.7 $\pm$ 0.5	103.7 $\pm$ 0.4	66.2 $\pm$ 0.7	30.0 $\pm$ 0.5
0.83	104.8 $\pm$ 0.4	97.5 $\pm$ 0.3	59.2 $\pm$ 0.6	29.2 $\pm$ 0.5
0.98	96.9 $\pm$ 0.7	87.0 $\pm$ 0.4	45.9 $\pm$ 0.4	-

Note. The PV was located in front with a channel depth of 0.2 m. Readings were taken each second during all flow measurements. The RMSE of the readings is shown behind the plus minus symbol ( $\pm$ ). The horizontal location of each thermocouple is depicted in Figure 6.

Abbreviations: PV, photovoltaics; MDF, medium-density fiber; RMSE, root mean square error.

maximum difference of 6 K between the measurement of the PVF layout with a cavity depth of 0.1 m and the PVI layout located in the middle of a 0.48-m chimney cavity. A lower ambient temperature increases the difference in temperature with respect to the air within the cavity. This results in higher mass flow. However, in the experiment, this effect was found negligible compared with the effects of the cavity depth.

### Air humidity measurements

According to Zhang et al.,<sup>29</sup> the difference in the value of the Nusselt number for dry air contained within a channel at 77 $^{\circ}\text{C}$  average temperature, with 50% humid air under the same conditions, is close to 1%. As Table 6 shows, such difference in humidity was never achieved; therefore, the effect on the Nusselt number can be considered negligible.

### Surface temperatures

For the sake of brevity, only two layouts will be discussed in this section: a PVF with 0.2 m cavity and a PVI with a PV module located in the middle of a 0.2-m cavity (ie, two sub-cavities of 0.1 m each). Surface temperatures were measured and then averaged over the entire duration of the activity. The RMSE was calculated and analyzed to see the effect of the different layouts. Table 7 shows the temperatures of the PVF, on both the front layer (the PV module) and the back layer (the building material, here MDF). The seven temperatures belong to each thermocouple located on each layer as depicted by Figure 6.

A vertical gradient of temperatures (lower on the bottom, higher on the top) is expected. However, the nonhomogeneous nature of the LASS irradiance, as shown in Table 3, produces a similar pattern in temperatures on the front surface of the PV module as that of the irradiance measured.

**TABLE 8** The average temperature ( $^{\circ}\text{C}$ ) readings of the thermocouples placed on the surface of each layer

Distance From Top, m	Glass		PV		MDF	
	Front T, $^{\circ}\text{C}$	Back T, $^{\circ}\text{C}$	Front T, $^{\circ}\text{C}$	Back T, $^{\circ}\text{C}$	Front T, $^{\circ}\text{C}$	Back T, $^{\circ}\text{C}$
0.04	75.8 $\pm$ 0.2	88.0 $\pm$ 0.3	89.2 $\pm$ 0.2	88.1 $\pm$ 0.3	60.7 $\pm$ 0.3	-
0.19	81.1 $\pm$ 0.2	97.1 $\pm$ 0.3	101.1 $\pm$ 0.2	96.2 $\pm$ 0.3	66.1 $\pm$ 0.3	31.6 $\pm$ 0.2
0.35	84.2 $\pm$ 0.2	98.1 $\pm$ 0.4	100.9 $\pm$ 0.2	92.9 $\pm$ 0.3	63.5 $\pm$ 0.3	31.4 $\pm$ 0.2
0.51	88.4 $\pm$ 0.2	91.9 $\pm$ 0.3	97.3 $\pm$ 0.2	90.3 $\pm$ 0.3	61.4 $\pm$ 0.3	30.8 $\pm$ 0.2
0.67	84.1 $\pm$ 0.3	84.0 $\pm$ 0.3	90.4 $\pm$ 0.2	84.8 $\pm$ 0.2	56.1 $\pm$ 0.4	30.0 $\pm$ 0.2
0.83	72.8 $\pm$ 0.4	75.5 $\pm$ 0.3	79.9 $\pm$ 0.2	75.6 $\pm$ 0.2	48.2 $\pm$ 0.5	29.1 $\pm$ 0.2
0.98	66.0 $\pm$ 0.4	61.1 $\pm$ 0.3	65.8 $\pm$ 0.2	60.9 $\pm$ 0.3	45.6 $\pm$ 0.3	-

Note. The PV was located in the middle of 0.2 m producing two channels of 0.1 m. Readings were taken each second during all flow measurements. The RMSE of the readings is shown behind the plus minus symbol ( $\pm$ ). The horizontal location of each thermocouple is depicted in Figure 6.

Abbreviations: MDF, medium-density fiber; PV, photovoltaics; RMSE, root mean square error.

For the case of the PVI with a 0.2-m cavity depth, the surface temperatures can be found in Table 8. Similar to the PVF case, an increasing temperature gradient is formed from the bottom to the top. Temperature of the PV module is lower than that in the case of the PVF. The reasons for this are the following: First, the LASS solar simulator produced a significant amount of infrared radiation (as discussed earlier). The front glass absorbs a relatively large quantity of it (27%). For the case of the PVF, all this radiation reaches directly the PV module. Second, the first layer on all the experiments was located very close to the LASS solar simulator, which produces higher radiative temperature from the environment, and this condition will not occur under real ambient conditions.

### Anemometer temperature profiles

Air temperature profiles across the cavity for both layouts were measured with the anemometer and compared with those of the nearest surface thermocouple. The cavity geometry, the layout of both configurations, and the profiles obtained are depicted in Figure 7 for the PVF and Figure 8 for the PVI. Thermal boundary layers are clearly visible on both cases. For the PVI layout, the air temperature at the middle of

both cavities is higher than the air temperature at the middle of the PVF cavity. Lower air volume and higher surface temperatures on the surfaces forming channel 1 (front glass and PV) are the cause of this difference. Channel 2 (PV and MDF) shows surface temperatures lower than in the PVF case, but the horizontal temperature profile is higher. High velocity is the reason behind this difference, as it will be shown later.

### Velocity profiles

Velocity profile measurements are shown in Figure 9 for the PVF with 0.2 m cavity and in Figure 10 for the PVI with 0.2 m cavity and the PV module in the middle. The reader is advised to note the difference on the scale of the y-axis between Figures 9 and 10. Center velocity is larger in channel 1 when compared with that in the other cavities and shows close symmetry in shape with its temperature profile. It is also clear that the higher the surface temperature on a layer, the higher the velocity of air near its boundary. The air velocity in channel

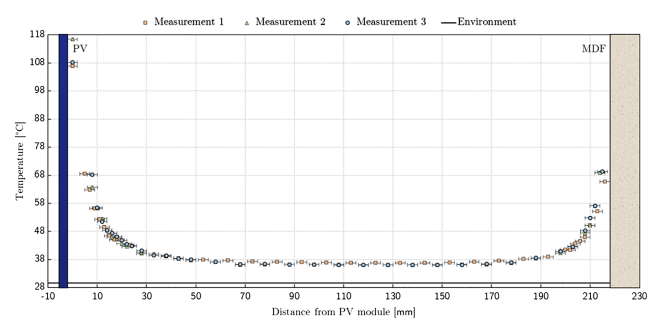


**FIGURE 7** The temperature profile of air for PV located in the front with a channel depth of 0.2 m. The air temperature is measured 0.1 m below the exit of the channel. The data points closest to the sketched layers are surface temperatures from the thermocouple located 0.19 m from the top. PV, photovoltaics [Colour figure can be viewed at wileyonlinelibrary.com]

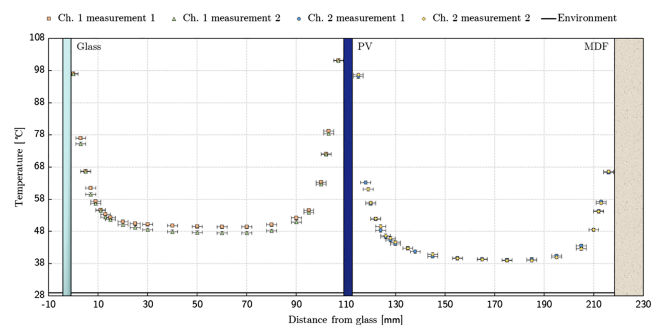


**FIGURE 8** The temperature profile of air for the PV located in the middle with channel depths of, respectively, 0.1 and 0.1 m. The air temperature is measured 0.1 m below the exit of the channel. The data points closest to the sketched layers are surface temperatures from the thermocouple located 0.19 m from the top. Channel 1 is the air channel between glass and PV; channel 2 is between PV and MDF. MDF, medium-density fiber; PV, photovoltaics [Colour figure can be viewed at wileyonlinelibrary.com]

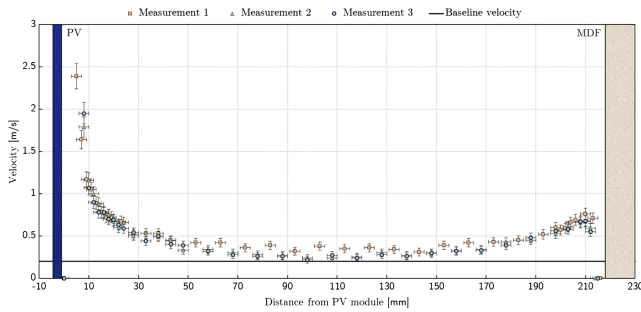


**FIGURE 9** The velocity profile of the PV located in the front with a channel depth of 0.2 m, measured 0.1 m below the exit of the channel. The data points in the extremes of the x axis are zero values representing the “no slip” boundary condition on the surface of the PV module and the MDF layer. MDF, medium-density fiber; PV, photovoltaics [Colour figure can be viewed at wileyonlinelibrary.com]

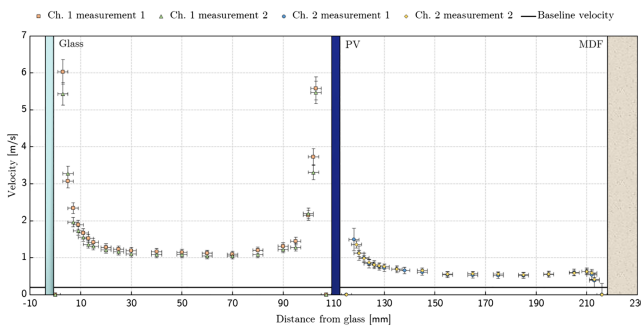


**FIGURE 10** The velocity profile of the PV located in the middle with channel depths of 0.1 m, respectively, 0.1 m, measured 0.1 m below the exit of the channel. The data points in the extremes of the x axis are zero values representing the “no slip” boundary condition on the surface of the glass and the PV module. MDF, medium-density fiber; PV, photovoltaics [Colour figure can be viewed at wileyonlinelibrary.com]

1 is almost three times that of channel 2, despite having the same depth, owing to their difference in temperature.

**Heat flow**

Integrating the product of density, velocity, and temperature difference gives the convective heat flow through the channel. Owing to the nature of the data, trapezoidal integration was used, and the convective heat flow is, therefore, given by

$$\dot{Q}' = c_p \sum_{i=1}^N \frac{\rho(T_{i-1})v_{i-1}[T_{i-1} - T_e] + \rho(T_i)v_i[T_i - T_e]}{2} \Delta x_i. \quad (34)$$

Thermophysical properties of air were obtained by linear interpolation on a lookup table similar to that of Rheault and Bilgen.<sup>11</sup> Given that humidity was considered negligible, dry air properties were used and specific heat was assumed constant and equal to 1007 J/kg K. The heat flow is unidirectional given that across the width of the layers all properties were considered constant. Table 9 shows the results for all the topologies measured.

**TABLE 9** The heat flow and respective progressed RMSE of different topologies

Topology	$\dot{Q}'$ Channel 1, W/m	$\dot{Q}'$ Channel 2, W/m	$\dot{Q}'$ Total, W/m
PVF 0.4 m	1592±99	-	1592±99
PVF 0.2 m	1396±109	-	1396±109
PVF 0.1 m	1411±145	-	1411±145
PVI 0.2, 0.2 m	3020±162	457±56	3476±218
PVI 0.3, 0.1 m	2864±114	686±33	3550±147
PVI 0.1, 0.3 m	4438±47	394±65	4832±112
PVI 0.1, 0.1 m	4895±64	750±25	5646±89

Note. The values in red are physically impossible. It is assumed that the irradiance incident on the anemometer significantly increased its readings. Abbreviations: PVF, photovoltaics as front layer; PVI, photovoltaics located inside; RMSE, root mean square error.

It can be observed that the incident heat, provided by the LASS solar simulator, is lower than the heat flux in channel 1. This is thermodynamically impossible. The reason for this discrepancy is the influence of direct irradiance on the anemometer. It can be seen that the values of heat flux in channel 2 is far more consistent. On this channel, the anemometer is completely hidden from irradiance coming from the LASS. With this, the values highlighted in red were discarded and not used for validation or analysis. The exit temperature over each channel depth is shown in Table 10.

**Mass flow**

Trapezoidal integration of the product of velocity and density yields the total mass flow:

$$\dot{m}' = \sum_{i=1}^N \frac{\rho(T_{i-1})v_{i-1} + \rho(T_i)v_i}{2} \Delta x_i. \quad (35)$$

The results are summarized in Table 11 for all the topologies measured. Mass flow increases with channel depth for the PVF topology. However, as mentioned before, a maximum draught of 0.2 m/s was measured in the room. The value measured for the case of a cavity of 0.4 m in the PVF was of 0.15 m/s. It cannot be concluded if this flow is the product of the draught in the room, or any effect caused by the PVF at such depth. This same condition appears on the PVI layout, where channel 1 has a depth of 0.1 and channel 2 has a depth of 0.3. In this layout, the latter also produces a mass flow below the natural draught of the room.

For the case of the PVF, increasing the cavity depth from 0.1 to 0.2 m has a very small effect on the mass flow. However, using a similar depth and placing a PV module in the middle of the cavity more than double the flow. However, care should be taken since the front side measurements have been proven biased, as explained in Table 9. Looking only at channel 2 shows that the flow difference between both layouts is not large.

An analysis of the surface temperatures shows that for the case of the PVI, temperatures on both surfaces of the front glass and at the front surface of the PV module are larger than those of the back surface of the PV module and the MDF. This indicates that the mass

**TABLE 10** The exit temperatures and the environmental temperature including the RMSE for all topologies

Topology	$T_{\text{exit}}$ Channel 1, ° C	$T_{\text{exit}}$ Channel 2, ° C	$T_{\text{e}}$ , ° C
PVF 0.4 m	37.0±0.4	-	29.8±0.2
PVF 0.2 m	40.8±0.1	-	29.6±0.3
PVF 0.1 m	48.0±0.3	-	32.8±0.4
PVI 0.2, 0.2 m	46.5±1.9	37.1±0.1	27.9±0.4
PVI 0.3, 0.1 m	45.1±1.4	43.5±0.1	29.4±0.4
PVI 0.1, 0.3 m	52.6±0.7	35.4±0.1	26.9±0.4
PVI 0.1, 0.1 m	54.1±1.0	44.1±0.1	28.9±0.2

Abbreviations: PVF, photovoltaics as front layer; PVI, photovoltaics located inside; RMSE, root mean square error.

**TABLE 11** The mass flow per meter width and respective RMSE of different topologies

Topology	$\dot{m}'$ Channel 1, kg/sm	$\dot{m}'$ Channel 2, kg/sm	$\dot{m}'$ Total, kg/sm
PVF 0.4 m	0.14±0.00	-	0.14±0.00
PVF 0.2 m	0.11±0.01	-	0.11±0.01
PVF 0.1 m	0.09±0.01	-	0.09±0.01
PVI 0.2, 0.2 m	0.14±0.01	0.08±0.00	0.23±0.02
PVI 0.3, 0.1 m	0.15±0.00	0.06±0.00	0.21±0.00
PVI 0.1, 0.3 m	0.17±0.00	0.10±0.00	0.26±0.01
PVI 0.1, 0.1 m	0.17±0.01	0.07±0.00	0.24±0.01

Note. Channel 1 is the first channel from the front of the façade; channel 2 is the second channel.

Abbreviations: PVF, photovoltaics as front layer; PVI, photovoltaics located inside; RMSE, root mean square error.

flow on the first channel must be greater. Thus, the PVI layout yields higher mass flow than does the PVF.

### PV temperature

Given the important effect that temperature has on PV module performance, operating temperatures of the PV modules call for a separate analysis. Table 12 shows the average temperatures and RSME values for all the measured layouts.

**TABLE 12** The mean surface temperatures including the RMSE of the PV module for different topologies

Topology	Mean PV Front T, ° C	Mean PV Back T, ° C
PVF 0.4 m	112.5±0.8	103.0±0.8
PVF 0.2 m	109.5±0.6	102.8±0.6
PVF 0.1 m	109.6±0.3	108.0±0.3
PVI 0.2, 0.2 m	83.8±0.4	78.6±0.4
PVI 0.3, 0.1 m	82.5±0.3	78.3±0.3
PVI 0.1, 0.3 m	85.7±0.4	79.9±0.5
PVI 0.1, 0.1 m	90.2±0.2	84.9±0.3

Abbreviations: PV, photovoltaics; PVF, photovoltaics as front layer; PVI, photovoltaics located inside; RMSE, root mean square error.

It can be seen that as the cavity depth increases for the case of the PVF, the differences in temperatures become smaller. Going from a depth of 0.2 to 0.4 m, the variation of the back surface temperature in the PV module does not change significantly.

For the PVI layout, a trend seems to be clear: The closer the PV module is to the front glass, the higher its surface temperatures, both at the front and at the back. This applies to smaller depths in channel 1 more than in channel 2. In the latter case, since the temperature of the MDF is lower compared with the front glass temperature, the PV module temperature will be lower for smaller values of depth in channel 2.

It is important to remember that the LASS used induces a bias on the measurements. High infrared radiation and very small distance between the LASS and the front layer cause very large ambient temperature around the front layers, thus inducing effects not found on real-life applications.

## 4 | VALIDATION OF COMPUTATIONAL MODEL

### 4.1 | Irradiance model

The model created for the incident irradiance was compared with a similar system using the System Advisor Model (SAM), a validated model created by National Renewable Energy Laboratory (NREL).<sup>30</sup> As it can be seen in Figure 15, both the direct and diffuse components on the plane of array are in good accordance with SAM results, which are validated models by NREL.

The root mean square difference of the model compared with SAM is 0.4%.

### 4.2 | Control volume model and mass flow model

Once the irradiance model was validated, inputs from the experimental setup were used on the control model and mass flow model to study their accuracy. Mean irradiance measured at the location of the thermocouples was used as input. Other relevant input variables are summarized in Table 13. The time taken by the setup to reach steady state was less than 3 hours.

**TABLE 13** Input parameters used to model the experimental conditions

Input Variable	Value	Unit
Vertical control volumes	14	-
Horizontal control volumes per layer	5	-
Irradiance	1664.8	W/m <sup>2</sup>
Angle of incidence	0	deg
Roughness	0.0002	m
Time	3	h
Timestep	100	s

**Mass flow model**

Given that the results for the PVF are calculated in nondimensional form, they are suitable for comparison with other studies with similar layouts. Ambient temperature was used to calculate all the relevant properties of air. The modified Rayleigh number was obtained via Equation (36).

$$Ra^* = \left( \frac{g\beta H^4 q}{avk} \right) \frac{d}{H} \tag{36}$$

With this modified Rayleigh number, the results were compared with those of other relevant studies. Of those studies, the work of Liu et al<sup>25</sup> was the only one in which an artificial light source is used. The results obtained are strongly correlated to those of Liu. Other data sets also show a strong correlation with the modified Rayleigh number, but their gradients change from one another. Figure 11 shows that the model can accurately model the mass flow of the PVF layout. It is important to notice that, in Figure 11, the data from

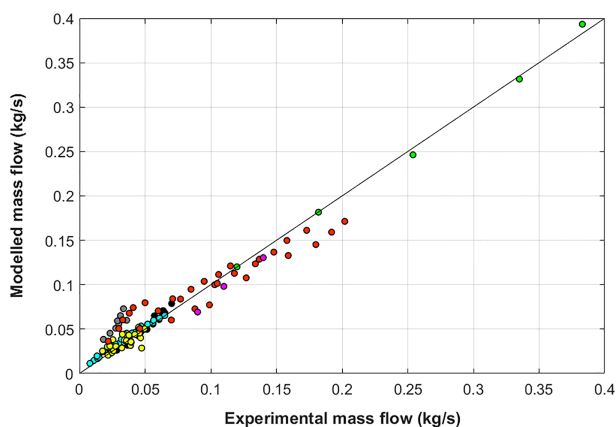


**FIGURE 11** Modeled vs measured mass flow for multiple experimental data sets including the current research in kg/s. The current research values represent the PVF layout. The studies shown in this graph are as follows: green,<sup>22</sup> grey,<sup>20</sup> yellow,<sup>26</sup> cyan,<sup>23</sup> and black<sup>21</sup>; red belongs to Liu et al<sup>25</sup> with the modified correction presented on this work. Finally, magenta is the results of the experiments carried in this work [Colour figure can be viewed at wileyonlinelibrary.com]

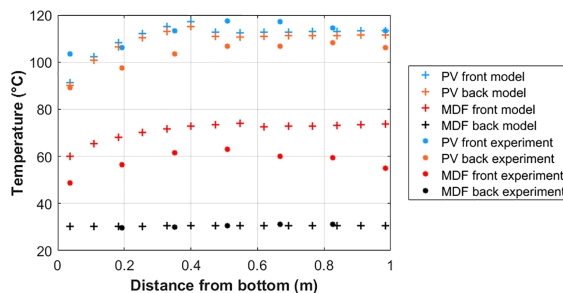


**FIGURE 12** Local surface temperatures at each vertical position starting from the bottom for a PVF layout with a cavity depth of 0.4 m, modeled under homogeneous irradiance. MDF, medium-density fiber layer; PV, photovoltaics; PVF, photovoltaics as front layer [Colour figure can be viewed at wileyonlinelibrary.com]

Liu et al<sup>25</sup> were calculated with the correction factors presented in this work. Given that measurements for the layout of the PV module inside(PVI) produced a thermodynamically impossible scenario, owing to the significant impact that the irradiance from the LASS had on the anemometer, the validation for this layout could not be carried out.

**4.2.1 | Local surface temperature**

Vertical temperature profiles were calculated for each layer and compared with the measurements obtained. Figures 12 and 13 show the vertical profiles for the PVF and PVI layout, respectively. In the former, the cavity depth was considered as 0.4 m. In the latter, the PV module was located at 0.1 m from the front glass and 0.3 m from the back surface. A good agreement for the temperature profiles of the back of the MDF surface and the front of the MDF surface on the PVI layout was observed for both experiments. The temperature of the front and back of the PV module is almost nondependent on distance, whereas in the experiment, a clear dependency is observed. This could be due to the simplification of the thermal resistance of the module, which is modeled by a single thermal resistance. Individual layer resistances were not considered. From the graphs, at 0.4 m from the bottom, a

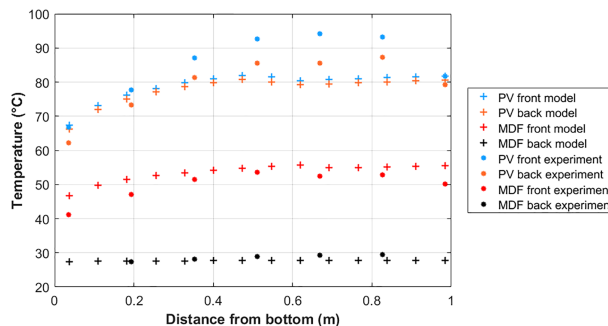


**FIGURE 13** Local surface temperatures at each vertical position starting from the bottom for a PVI layout with channel depths of 0.1 m (channel 1) and 0.3 m (channel 2), modeled under homogeneous irradiance. MDF, medium-density fiber layer; PV, photovoltaics; PVF, photovoltaics as front layer [Colour figure can be viewed at wileyonlinelibrary.com]

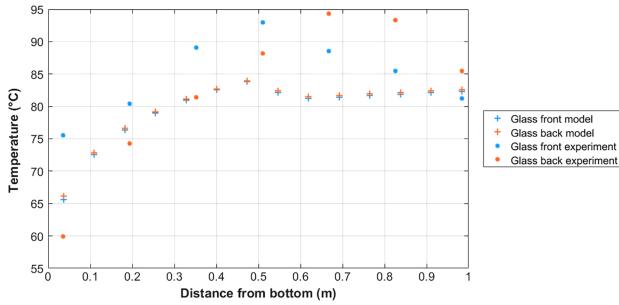


**FIGURE 14** Local surface temperatures at each vertical position starting from the bottom for the front glass of the PVI layout, modeled under homogeneous irradiance. PVI, photovoltaics located inside [Colour figure can be viewed at wileyonlinelibrary.com]

concave behavior is observed, indicating the transition from laminar to turbulent flow. For the case of the PVI, front layer glass surface is plotted separately and can be found in Figure 14.

Transient behavior was also compared for the different layouts (Figure 15). The model presents a good agreement with the front side of the PV module on the PVF case, an overestimation of the MDF front surface, and a back MDF surface temperature difference that gets smaller with time (Figure 16). This last difference might be improved if the ambient temperature is also varied with time and not considered fixed as in the model. Given the high power output of the LASS, the environmental temperature increased over time.

For the PVI layout, an underestimation of the front PV temperature is observed and a better agreement of the front MDF front layer temperature, as depicted by Figure 17.

#### 4.2.2 | Average values and RMSE

Convective heat flows were calculated by

$$\dot{q} = c_p(T_{\text{exit}} - T_e)\dot{m}. \quad (37)$$

All the results are summarized in Table 14.

Differences between the model and measurements for each layout are depicted in Table 15.

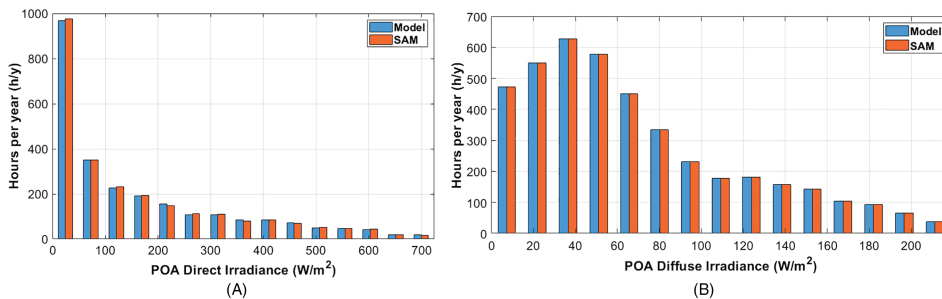


**FIGURE 15** A typical mean year weather file from weather station in Bilt, the Netherlands, is used to model the expected direct (A) and diffuse (B) irradiance on a south-oriented vertical wall. The results of the current model are compared with the results produced by the NREL-SAM using an equal orientation and the same weather file. NREL, National Renewable Energy Laboratory; POA, plane of array irradiance; SAM, System Advisor Model [Colour figure can be viewed at wileyonlinelibrary.com]

Relative RMSE values were obtained by dividing the absolute RMSE by the mean of the measurement values. RMSE for temperatures was calculated with the mean of the difference in temperature relative to environment. With respect to temperatures, the RMSE value is 5.27° C. PV temperatures were 4.66° C. Mass flow was 0.014 kg/s. Lastly, convective heat flow presented the largest RMSE value, with 407 W. The models tend to underestimate the heat flow on both layouts.

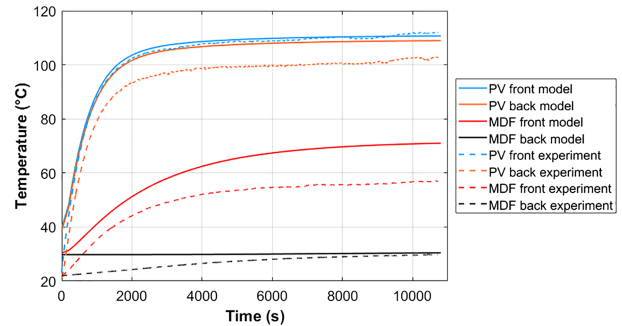


**FIGURE 16** Transient behavior of the temperatures at the different surfaces on a PVF layout. MDF, medium-density fiber layer; PV, photovoltaics; PVF, photovoltaics as front layer [Colour figure can be viewed at wileyonlinelibrary.com]

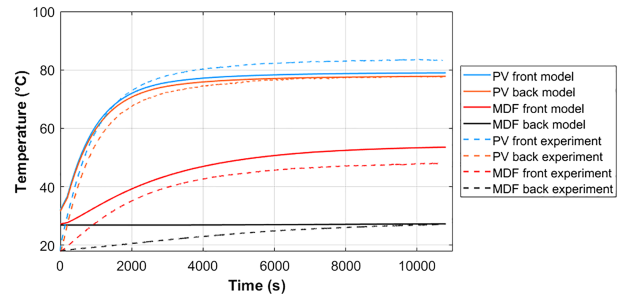


**FIGURE 17** Transient behavior of the temperatures at the different surfaces on a PVI layout. MDF, medium-density fiber layer; PV, photovoltaics; PVF, photovoltaics as front layer [Colour figure can be viewed at wileyonlinelibrary.com]

**TABLE 14** Model results of average surface temperatures, exit air flow temperatures, mass flows, and heat flows per meter width

Topology	T, °C Air 1	T, °C Air 2	T, °C Glass f	T, °C Glass b	T, °C PV f	T, °C PV b	T, °C MDF f	T, °C MDF b	m', kg/sm Air 1	m', kg/sm Air 2	q', W/m Air 1	q', W/m Air 2
PVF 0.4	36.1				110.7	108.9	71.0	30.4	0.14		886	
PVF 0.2	38.4				110.4	108.7	75.0	30.3	0.10		890	
PVF 0.1	47.1				115.3	113.7	83.2	33.6	0.06		882	
PVI 0.2, 0.2	35.1	33.7	79.4	79.3	78.8	77.8	55.5	28.3	0.09	0.08	675	480
PVI 0.3, 0.1	35.5	38.6	80.8	80.7	80.7	79.7	59.5	29.9	0.11	0.05	687	468
PVI 0.1, 0.3	38.4	31.8	79.6	79.5	79.0	77.8	53.6	27.3	0.06	0.10	655	495
PVI 0.1, 0.1	40.6	38.4	82.1	82.1	81.9	80.8	59.9	29.4	0.06	0.05	665	488

Note. f stands for the front surface of the layer, b stands for the back surface, 1 stands for the front air channel, and 2 stands for the back air channel. Abbreviations: PVF, photovoltaics as front layer; PVI, photovoltaics located inside.

**TABLE 15** Model difference of average surface temperatures, exit air flow temperatures, mass flows, and heat flows per meter width when compared with the experiment

Topology	ΔT, K Air 1	ΔT, K Air 2	ΔT, K Glass f	ΔT, K Glass b	ΔT, K PV f	ΔT, K PV b	ΔT, K MDF f	ΔT, K MDF b	m', kg/sm Air 1	m', kg/sm Air 2	q', W/m Air 1	q', W/m Air 2
PVF 0.4	-0.9				-1.8	5.9	12.7	-0.1	-0.00		-705	
PVF 0.2	-2.4				0.9	5.9	11.5	0.0	-0.01		-506	
PVF 0.1	-0.9				5.7	5.7	18.2	0.7	-0.03		-529	
PVI 0.2, 0.2		-3.4	-5.6	-0.3	-5.0	-0.8	3.9	-0.9		0.00		23
PVI 0.3, 0.1		-4.9	-0.7	3.0	-1.8	1.4	5.4	-1.1		-0.01		-218
PVI 0.1, 0.3		-3.6	-5.7	-3.7	-6.7	-2.1	3.4	-1.3		-0.00		102
PVI 0.1, 0.1		-5.7	2.5	-3.9	-8.3	-4.1	2.2	-1.1		-0.02		-263

Note. f stands for the front surface of the layer, b stands for the back surface, 1 stands for the front air channel and 2 stands for the back air channel. Abbreviations: PVF, photovoltaics as front layer; PVI, photovoltaics located inside.

**TABLE 16** Modeled input variables for a PVF chimney and a PVI chimney

Variable	PVF	PVI
Orientation	South (180°)	South (180° )
Height, m	10	10
Width, m	10	10m
Material 1	PV	glass
Depth material 1, m	0.008	0.008
material 2	Brick masonry	PV
Depth material 2, m	0.1	0.008
Material 3	Mineral wool	Brick masonry
Depth 3, m	0.06	0.1
Material 4	Brick masonry	Mineral wool
Depth 4, m	0.1	0.06
Material 5	-	Brick masonry
Depth 5, m	-	0.1

Abbreviations: PVF, photovoltaics as front layer; PVI, photovoltaics located inside.

## 5 | PERFORMANCE OF A PV CHIMNEY: SENSITIVITY ANALYSIS

The performance of a PV chimney was carried out by comparing both topologies, PVF and PVI, for a three-story construction in Amsterdam, the Netherlands. The façade size, on both cases, was assumed to be 10 m by 10 m, oriented towards the south. The input variables for the models are summarized in Table 16.

The model was used to perform a basic sensitivity analysis of the heat flow generation and electricity production for both the PVF and PVI cases. The first step was to study the effect of the channel depth on both variables. The depth was varied from 0.2 to 1.02 m in steps of 0.04 m. It was found that at smaller depths, heat flow generation changed significantly until it reached a plateau at 0.2 m. From this depth onward, the increase on heat flows grows slightly until a depth value of 0.4 m. The PVI, owing to its configuration, presents a higher heat flow than does the PVF (see Figure 18A). However, the PV modules on the PVI layout work at higher temperatures than in the PVF layout, which reduces their electrical performance, as can be seen in Figure 18B.

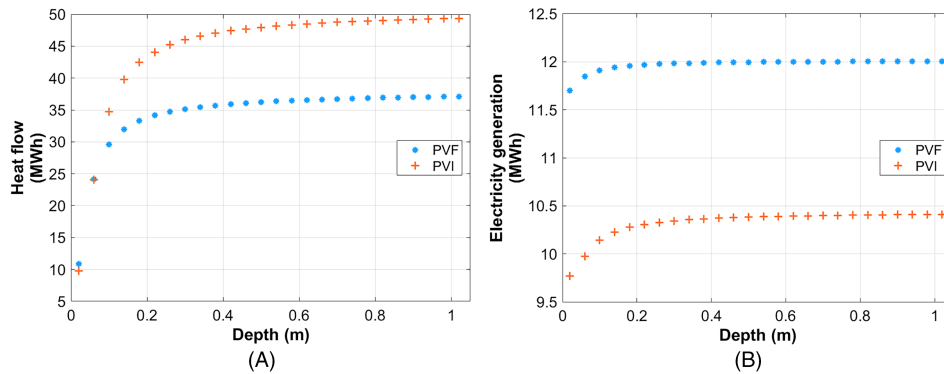


**FIGURE 18** Yearly heat flow (A) and electricity (B) generation for a PVF and PVI as function of channel depth. PVF, photovoltaics as front layer; PVI, photovoltaics located inside [Colour figure can be viewed at [wileyonlinelibrary.com](http://wileyonlinelibrary.com)]

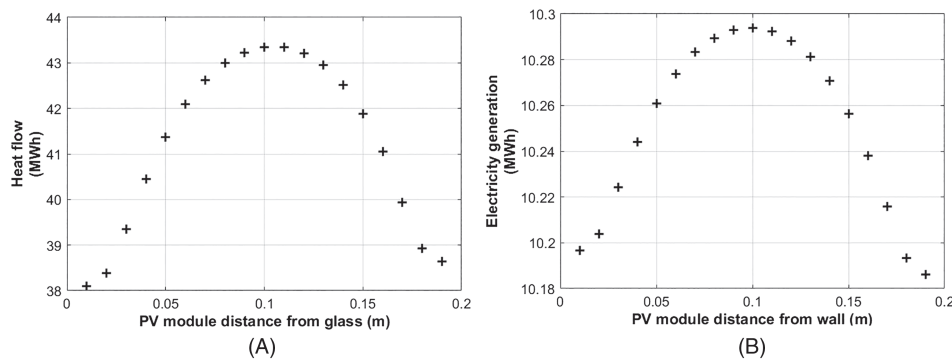


**FIGURE 19** Yearly heat flow (A) and electricity (B) generation for different locations of the PV module within the cavity depth for the PVI layout. PVF, photovoltaics as front layer; PVI, photovoltaics located inside

For the PVI case, simulations were performed with the aim to find the best position of the PV module inside the channel. As in the case of the cavity depth, both yearly heat flow and electricity production were studied. The modules were located from 0.01 m from the front glass to 0.01 m from the masonry wall with steps of 0.01 m. An optimum for yearly heat flow production was found when the PV modules were located near the middle of the cavity, slightly closer to the front glass (see Figure 19A). To maximize yearly electricity production, the middle of the cavity also yields the highest values, slightly closer to the masonry wall (see Figure 19B). Overall, the optimum placing of the PV modules is in the middle of the cavity, at 0.1 m.

Further improvements for this model include complete modeling of the electrical and heat demand of households as function of their built areas; inclusion of the effect of the ambient wind speed; and automatic design optimization of a PVF or PVI that includes orientation, height, width, and cavity depth based on meteorological data for the location at which the technology is to be implemented.

## 6 | CONCLUSIONS

A new modeling method for the combination of two building energy methods, the PVF and the PVI of an integrated chimney, has been

proposed and validated with experimental data. The user has the ability to provide inputs of meteorological conditions of the desired installation location, materials to be used, geometry of the double façade, and the specifications of the PV module chosen. The model calculates the resulting POA irradiance, temperature profiles, mass flow, and heat flow.

The relative RMSE of temperature, PV temperature, mass flow, and heat flow were found to be 14.6%, 7.3%, 14.9%, and 42.7%, respectively. Thus, it was found that both the PVF and PVI layouts could be modeled by a 2D control volume thermal model. The heat flow could also be modeled, although care should be taken regarding its accuracy.

A relative root mean square deviation (RMSD) of 0.4% was found when comparing the irradiance model of this study with the irradiance model of SAM.<sup>30</sup>

A sensitivity analysis was conducted to find the effect of channel depth on the heat and electricity production of a PVF/PVI layout. An optimum cavity for the PVF layout is expected between 0 and 0.1 m. The generation of electricity by the PV modules within a PVI layout was found to increase at positions closer to the building wall, whereas the heat flow increased at positions closer to the front glass. The optimum location for the PV module in the channel for the base case (total channel depth of 0.2 m) was found to be in the middle, at 0.1 m.

**NOMENCLATURE**

## Latin letters

<i>a</i>	Thermal diffusivity $m^2/s$
$A_T$	Altitude deg
$A_Z$	Azimuth deg
<i>b</i>	Correction factor -
$c_p$	Specific heat capacity at constant pressure $J/(kg K)$
<i>d</i>	Depth of the air channel m
$d_h$	Hydraulic diameter m
<i>e</i>	Error Variable
<i>F</i>	View factor -
<i>f</i>	Darcy friction coefficient for channel flows -
<i>G</i>	Irradiance $W/m^2$
<i>g</i>	Gravity constant $m/s^2$
<i>H</i>	Height of the air channel m
<i>h</i>	Heat transfer coefficient $W/(m^2 K)$
<i>I</i>	Effective irradiance, considering reflective losses $W/m^2$
<i>K</i>	Friction coefficient -
<i>k</i>	Thermal conductivity $W/(m K)$
<i>m</i>	Mass kg
<i>N</i>	Number of control volumes -
<i>P</i>	Power W
<i>Q</i>	Energy J
<i>q</i>	Energy per area $J/m^2$
<i>r</i>	Reflectance of perpendicular or polarized light -
<i>T</i>	Temperature K or °C
<i>v</i>	Velocity m/s
<i>x</i>	Local distance parallel to the flow m

## Greek letters

$\alpha$	Absorption coefficient $m^{-1}$
$\beta$	Thermal expansion coefficient $K^{-1}$
$\delta_T$	Thermal boundary layer m
$\epsilon$	Emissivity -
$\eta$	Efficiency -
$\Lambda$	Albedo -
$\nu$	Kinematic viscosity $m^2/s$
$\rho$	Density $kg/m^3$
$\theta$	Angle of incidence deg
$\zeta$	Plume depth to channel depth ratio -

## Nondimensional numbers

<i>Gr</i>	Grasshof number
<i>Nu</i>	Nusselt number
<i>Pr</i>	Prandtl number

## Diacritics

'	per meter width
·	per second
·	mean

## Subscripts

ab	Absorbed
----	----------

ch	Channel
exit	Channel exit
e	Environment
gl	Glass layer
inl	Inlet
L	Chimney layer
po	P polarization
PV	PV layer
p	Plume
s	Perpendicular
t	Transmitted
c	Convective
k	Conductive
M	PV module
r	Radiative
s	Sun
v	Vertical
x	x is used as specific length
1N	Individual control volume
sc	Solar cell

## Superscripts

dif	Diffuse
dir	Direct
gr	Ground

## Abbreviations

AOI	angle of incidence
POA	plane of array
RMSE	root mean square error

**ACKNOWLEDGEMENTS**

The authors will like to acknowledge Dr. R. Delfos and all the technical staff from architecture faculty of Delft University of Technology for their expertise on measurement and experimental setups of this nature, their knowledge on sensor selection, placement, and data logging, which were instrumental. Also, Stefaan Hermaan and Martijn Tijssen and Elias Garcia Goma are thanked for their technical expertise of the Photovoltaic Laboratory used during this work.

**ORCID**

Juan Camilo Ortiz Lizcano  <https://orcid.org/0000-0002-0165-5493>

**REFERENCES**

- Green MA, Emery K, Hishikawa Y, Warta W, Dunlop ED. Solar cell efficiency tables (version 45). *Prog Photovolt Res Appl*. 2015;23(1):1-9.
- Maturi L, Belluardo G, Moser D, Del Buono M. BIPV system performance and efficiency drops: overview on PV module temperature conditions of different module types. *Energy Procedia*. 2014;48:1311-1319.
- Abdelrazik AS, Al-Sulaiman F, Saidur R, Ben-Mansour R. A review on recent development for the design and packaging of hybrid

- photovoltaic/thermal (PV/T) solar systems. *Renew Sust Energy Rev.* 2018;95:110-129.
4. Farkas K, Munari Probst MC, Horvat M. Barriers and Needs for Building Integration of Solar Thermal and Photovoltaics. <http://infoscience.epfl.ch/record/162426>; 2010.
  5. Scognamiglio A, Røstvik HN. Photovoltaics and zero energy buildings: a new opportunity and challenge for design. *Progr Photovolt: Res Appl.* 2013;21(6):1319-1336.
  6. Nowak S, Gutschner M, Ruoss D, Togweiler P, Schoen T. Potential for building integrated photovoltaics. Report IEA-PVPS T7-4; 2002.
  7. Harris D, Helwig N. Solar chimney and building ventilation. *Appl Energy.* 2007;84(2):135-146.
  8. Oesterle E, Lieb, Lutz, Heusler. *Double-Skin Facades.* Illustrate: Prestel; 2001.
  9. Von Grabe J.. Flow resistance for different types of windows in the case of buoyancy ventilation. *Energy Build.* 2013;65:516-522. <https://doi.org/10.1016/j.enbuild.2013.06.035>
  10. Balocco C. A non-dimensional analysis of a ventilated double façade energy performance. *Energy Build.* 2004;36(1):35-40.
  11. Rheault S, Bilgen E. Heat transfer analysis in an automated venetian blind window system. *J Sol Energy Eng.* 1989;111(1):89. <http://solarenergyengineering.asmedigitalcollection.asme.org/article.aspx?articleid=1454866>
  12. Gratia E, De Herde A. Greenhouse effect in double-skin facade. *Energy Build.* 2007;39(2):199-211.
  13. Ioannidis Z, Buonomano A, Athienitis AK, Stathopoulos T. Modeling of double skin façades integrating photovoltaic panels and automated roller shades: analysis of the thermal and electrical performance. *Energy Build.* 2017;154:618-632. <http://linkinghub.elsevier.com/retrieve/pii/S0378778817317851>
  14. De Gracia A, Castell A, Navarro L, Oró E, Cabeza LF. Numerical modeling of ventilated facades: a review. *Renew Sust Energy Rev.* 2013;22:539-549.
  15. Wong SC, Chu SH, Ai MH. Revisit on natural convection from vertical isothermal plate arrays II 3-D plume buoyancy effects. *Int J Therm Sci.* 2018;126(January):205-217. <https://doi.org/10.1016/j.ijthermalsci.2018.01.008>
  16. Smets AH, Isabella O, Zeman M, et al. *Solar Energy: The Physics and Engineering of Photovoltaic Conversion Technologies and Systems:* UIT; 2016.
  17. Shelby JE. *Introduction to Glass Science and Technology:* RSC Publishing; 2005.
  18. Haedrich I, Surve S, Thomson A. Cell to module (CTM) ratios for varying industrial cell types. In: 2015 Asia Pacific Solar Research Conference; 2015:1-6. [http://apvi.org.au/solar-research-conference/wp-content/uploads/2015/12/I-Haedrich\\_Peer-Reviewed\\_FINAL.pdf](http://apvi.org.au/solar-research-conference/wp-content/uploads/2015/12/I-Haedrich_Peer-Reviewed_FINAL.pdf)
  19. Cotfas DT, Cotfas PA, Machidon OM. Study of temperature coefficients for parameters of photovoltaic cells. *Int J Photoenergy.* 2018;2018(4):1-12. <https://doi.org/10.1155/2018/5945602>
  20. Chen ZD., Bandopadhyay P, Halldorsson J, Byrjalsen C, Heiselberg P, Li Y. An experimental investigation of a solar chimney model with uniform wall heat flux. *Build Environ.* 2003;38(7).
  21. La Pica A, Rodonò G, Volpes R. An experimental investigation on natural convection of air in a vertical channel. *Int J Heat Mass Transf.* 1993;36(3).
  22. Moshfegh B, Sandberg M. Flow and heat transfer in the air gap behind photovoltaic panels. *Renew Sust Energy Rev.* 1998;2. [https://doi.org/10.1016/S1364-0321\(98\)00005-7](https://doi.org/10.1016/S1364-0321(98)00005-7)
  23. Burek SAM, Habeb A. Air flow and thermal efficiency characteristics in solar chimneys and Trombe Walls. *Energy Build.* 2007;39(2).
  24. Mathur J, Bansal NK, Mathur S, Jain M, Anupma. Experimental investigations on solar chimney for room ventilation. *Sol Energy.* 2006;80(8).
  25. Liu B, Ma X, Wang X, Dang C, Wang Q, Bennacer R. Experimental study of the chimney effect in a solar hybrid double wall. *Sol Energy.* 2015;115. <https://doi.org/10.1016/j.solener.2015.02.012>
  26. He G, Zhang J, Hong S. A new analytical model for airflow in solar chimneys based on thermal boundary layers. *Sol Energy.* 2016 10;136:614-621. <https://doi.org/10.1016/j.solener.2016.07.041> <http://linkinghub.elsevier.com/retrieve/pii/S0038092X16302997>
  27. Ryan D, Burek SAM. Experimental study of the influence of collector height on the steady state performance of a passive solar air heater. *Sol Energy.* 2010;84(9). <https://doi.org/10.1016/j.solener.2010.05.018>
  28. Ayinde TF, Said SAM, Habib MA. Experimental investigation of turbulent natural convection flow in a channel. *Heat Mass Transf.* 2006;42(3). <http://link.springer.com/10.1007/s00231-005-0017-2>
  29. Zhang J, Gupta A, Baker J. Effect of relative humidity on the prediction of natural convection heat transfer coefficients. *Heat Transfer Eng.* 2007 4;28(4):335-342. <http://www.tandfonline.com/doi/abs/10.1080/01457630601122823>
  30. Gilman P. Sam Photovoltaic Model Technical Reference. National Renewable Energy Lab.(NREL), Golden, CO (United States); 2015.

**How to cite this article:** Ortiz Lizcano JC, Haghghi Z, Wapperom S, et al. Photovoltaic chimney: Thermal modeling and concept demonstration for integration in buildings. *Prog Photovolt Res Appl.* 2019;1-18. <https://doi.org/10.1002/pip.3194>